Chemical Science

ROYAL SOCIETY OF CHEMISTRY

EDGE ARTICLE

View Article Online
View Journal | View Issue

Cite this: *Chem. Sci.*, 2021, **12**, 8411

All publication charges for this article have been paid for by the Royal Society of Chemistry

Strategic molecular design of *closo-ortho*-carboranyl luminophores to manifest thermally activated delayed fluorescence†

Dong Kyun You,‡ Hyunhee So,‡ Chan Hee Ryu, Mingi Kim and Kang Mun Lee *

In this paper, we propose a strategic molecular design of *closo*-*o*-carborane-based donor–acceptor dyad system that exhibits thermally activated delayed fluorescence (TADF) in the solution state at ambient temperature. Planar 9,9-dimethyl-9*H*-fluorene-based compounds with *closo*- and *nido*-*o*-carborane cages appended at the C2-, C3-, and C4-positions of each fluorene moiety (*closo*-type: **2FC**, **3FC**, **4FC**, and **4FCH**, and *nido*-type: *nido*-**4FC** = [*nido*-form of **4FC**]·[NBu_4]) were prepared and characterized. The solid-state molecular structure of **4FC** exhibited a significantly distorted fluorene plane, which suggests the existence of severe intramolecular steric hindrance. In photoluminescence measurements, **4FC** exhibits a noticeable intramolecular charge transition (ICT)-based emission in all states (solution at 298 K and 77 K, and solid states); however, emissions by other *closo*-compounds were observed in only the rigid state (solution at 77 K and film). Furthermore, *nido*-**4FC** did not exhibit emissive traces in any state. These observations verify that all radiative decay processes correspond to ICT transitions triggered by *closo*-*o*-carborane, which acts as an electron acceptor. Relative energy barriers calculated by TD-DFT as dihedral angles around *o*-carborane cages change in *closo*-compounds, which indicates that the structural formation of **4FC** is nearly fixed around its S_0-optimized structure. This differs from that for other *closo*-compounds, wherein the free rotation of their *o*-carborane cages occurs easily at ambient temperature. Such rigidity in the structural geometry of **4FC** results in ICT-based emission in solution at 298 K and enhancement of quantum efficiency and radiative decay constants compared to those for other *closo*-compounds. Furthermore, **4FC** displays short-lived (~0.5 ns) and long-lived (~30 ns) PL decay components in solution at 298 K and in the film state, respectively, which can be attributed to prompt fluorescence and TADF, respectively. The calculated energy difference (ΔE_{ST}) between the first excited singlet and triplet states of the *closo*-compounds demonstrate that the TADF characteristic of **4FC** originates from a significantly small ΔE_{ST} maintained by the rigid structural fixation around its S_0-optimized structure. Furthermore, the strategic molecular design of the *o*-carborane-appended π-conjugated (D–A) system, which forms a rigid geometry due to severe intramolecular steric hindrance, can enhance the radiative efficiency for ICT-based emission and trigger the TADF nature.

Received 9th February 2021
Accepted 11th May 2021

DOI: 10.1039/d1sc00791b

rsc.li/chemical-science

Introduction

Recently, the icosahedral *closo-ortho*-carborane ($C_2B_{10}H_{12}$) cluster has gained popularity as an attractive functional component[1–4] because it can be considered as a stereoscopic analogue of a benzene ring owing to its high chemical stability and unique electronic characteristic. Furthermore, these properties lead to its extensive use as a three-dimensional unit for novel materials in the field of boron neutron capture therapy (BNCT),[2,5–7] building block-ligands of 60° vertex positioning,[8–14] and promising optoelectronic devices.[15–17] In particular, its strong electron withdrawing property, which originates from the high polarizability of its σ-aromaticity[18–22] *via* the high Lewis acidity of ten boron atoms in a cluster, provides the necessary impetus to reveal its intriguing photophysical properties when assembled with π-aromatic conjugated moieties.[3,4,15,23–59] These features of the *o*-carborane induce intramolecular charge transfer (ICT) transitions to form a donor (D)–acceptor (A) dyad system with aromatic groups, wherein *o*-carborane dominates orbital occupation in the excited state and plays the role of an electron acceptor.[23–45] Furthermore, the *o*-carborane-appended

Department of Chemistry, Institute for Molecular Science and Fusion Technology, Kangwon National University, Chuncheon, Gangwon, 24341, Republic of Korea. E-mail: kangmunlee@kangwon.ac.kr

† Electronic supplementary information (ESI) available: ^1H, $^1H\{^{11}B\}$, ^{13}C, and $^{11}B\{^1H\}$ NMR spectra, X-ray crystallographic data in CIF format, UV-vis absorption and PL spectra for *o*-carboranyl compounds and 9,9-dimethyl-9*H*-fluorene, emission decay curves, and computational calculation details. CCDC 2057685 for **2FC**, 2057686 for **3FC**, 2057688 for **4FC**, and 2057687 for **4FCH**, respectively. For ESI and crystallographic data in CIF or other electronic format see DOI: 10.1039/d1sc00791b

‡ The first and second authors contributed equally to this work.

D–A dyad compound exhibits specific emissive behavior during electronic relaxation based on ICT transition. Recent reports demonstrated that the ICT-induced emission is significantly affected by structural variations and molecular geometry. Fox *et al.* showed that the D–A dyad, *C*-diazaboryl-*o*-carborane, exhibits two different excited states (locally excited (LE) and ICT transition states), depending on the rotational motion of diazaboryl derivatives;[26] this phenomenon is called the twisted intramolecular charge-transfer (TICT) effect.[46–56] The occupation of the lowest unoccupied molecular orbital (LUMO) levels for an *o*-carborane cage is dramatically altered from 36% to 98% in accordance with the motion. This indicates that the electronic separation between the donor and acceptor moieties is governed by structural motion. Furthermore, our group reported that the structure of the molecular scaffold (*i.e.*, the planarity of the π-aromatic groups directly appended to the *o*-carborane cages) played a dominant role in efficiently isolating the highest occupied molecular orbital (HOMO; occupied on the π-aromatic group) and LUMO (occupied on *o*-carborane) levels in the excited states; this helped further enhance the radiative decay of the ICT transition.[57–59]

These results are the distinct inspiration to verify that the *o*-carborane-appended π-aromatic luminophore exhibits thermally activated delayed fluorescence (TADF).[60–65] This is because most *closo*-*o*-carboranyl-based luminophores possess minimum orbital overlap between HOMO and LUMO levels in the excited states, which is essential for inducing the narrow energy difference between the first-exited singlet (S_1) and triplet (T_1) states and for manifesting TADF.[66–69] Indeed, carbazole-based *o*-carborane D–A-type dyad derivatives[17] and Ag(I)-cyclized *o*-carborane complexes[70] simultaneously possess aggregation-induced emission (AIE) and strong TADF capabilities with high photoluminescence quantum efficiencies in the solid state. However, the TADF characteristics of ICT-based emissions can be observed only in rigid (solid or at low temperature) states because the structural fluctuations of *closo*-*o*-carborane (such as C–C bond elongation and the rotational motion of the cages) severely interrupts the radiative decay process based on the ICT transition in the solution state at ambient temperature.[23–26,46,48,50,71–73] All previous reports suggest that the strategic molecular design for the D–A-type *o*-carboranyl appended π-conjugation system that retains its structural rigidity sufficiently under ambient conditions leads to efficient TADF nature in solution at room temperature. Thus far, to the best of our knowledge, there are no reported studies on *closo*-*o*-carboranyl luminophores that exhibit a moderate TADF phenomenon in the solution state.

The effects of structural features and molecular geometry on the photophysical properties of *o*-carboranyl D–A conjugated systems have been previously reported. These studies provide strong evidence that emissive characteristics can be controlled *via* strategic molecular design. Specifically, a unique structural formation of appended π-aromatic groups on the *o*-carborane shows promise. By extension, previous findings demonstrated the promise of these conjugate systems as novel candidates for single-molecule visual sensing materials with a prompt emissive response.

To further examine this intrinsic concept to determine the relationship between the structural rigidity of *closo*-*o*-carboranyl luminophores and TADF, we strategically designed and synthesized planar fluorene-based *o*-carborane compounds (where biphenyl rings are anchored by a $C(CH_3)_2$ group) appended at the C2-(**2FC**), C3-(**3FC**), and C4-(**4FC**) positions of each fluorene moiety. Furthermore, a *nido*-*o*-carborane-type compound (*nido*-**4FC**) and its derivative (**4FCH**) that possesses a higher fluctuating geometry than that of **4FC** were prepared for comparing structural features and photophysical properties. Interestingly, the most rigid compound (**4FC**) exhibited moderate quantum efficiency and TADF nature in the solution state because of the small energy gap between the S_1 and T_1 states. This provides an insight into the strategic directivity of using *closo*-*o*-carboranyl conjugates as TADF materials. The detailed synthetic procedures, characterization, and optical properties (with theoretical calculations) have been described in this paper.

Experimental

General considerations

All operations were performed in an inert nitrogen atmosphere using standard Schlenk and glove box techniques. Anhydrous solvents (trimethylamine (NEt_3), toluene, tetrahydrofuran (THF), and dichloromethane (DCM); Sigma-Aldrich) were dried by passing them through an activated alumina column and stored over activated molecular sieves (5 Å). Spectrophotometric-grade solvents (methanol, ethyl acetate, and *n*-hexane) were used as received from Alfa Aesar. Commercial reagents purchased from Sigma-Aldrich (9,9-dimethyl-9*H*-fluorene, 2-bromo-9,9-dimethyl-9*H*-fluorene, 3-bromo-9,9-dimethyl-9*H*-fluorene, 4-bromo-9,9-dimethyl-9*H*-fluorene, phenylacetylene, ethynyltrimethylsilane, *n*-tetrabutylammonium fluoride, bis(triphenylphosphine)palladium(II) dichloride ($Pd(PPh_3)_2Cl_2$), copper(I) iodide (CuI), potassium carbonate (K_2CO_3), magnesium sulfate ($MgSO_4$), diethyl sulfide (Et_2S), and poly(methyl methacrylate) (PMMA)) and Alfa Aesar (decaborane ($B_{10}H_{14}$)) were used without any further purification. Dichloromethane-d_2 (CD_2Cl_2) purchased from Cambridge Isotope Laboratories was dried over activated molecular sieves (5 Å). All NMR spectra were recorded using a Bruker Avance 400 spectrometer (400.13 MHz for ^1H and $^1H\{^{11}B\}$, 100.62 MHz for ^{13}C, and 128.38 MHz for $^{11}B\{^1H\}$) at ambient temperature. Chemical shifts are expressed in ppm and referenced against external Me_4Si (^1H and ^{13}C) or $BF_3\cdot Et_2O$ (^{11}B). Elemental analyses were performed on an EA3000 instrument (EuroVector) at the Central Laboratory of Kangwon National University, respectively.

General synthetic routes for acetylene derivatives

All acetylene derivatives (**2FA**, **3FA**, **4FA**, and **4FASi**) were synthesized by following the scheme with an adequate amount of starting materials. Toluene (10 mL) and NEt_3 (10 mL) were added *via* a cannula to the mixture of bromo-fluorene precursors, CuI, and $Pd(PPh_3)_2Cl_2$ at 298 K. After stirring for 15 min,

phenylacetylene (for **2FA**, **3FA**, and **4FA**) or ethynyltrimethylsilane (for **4FASi**) of 2 equivalents per bromo-precursor was added to the resulting dark brown slurry. Then, the reaction mixture was refluxed for 24 h. Volatiles were removed with a rotary evaporator affording a dark gray residue. After washing with MeOH followed by *n*-hexane, the crude product was purified by column chromatography on silica gel ((eluent: DCM/*n*-hexane (1/20, v/v)) to afford acetylene derivatives.

Data for 9,9-dimethyl-2-(phenylethynyl)-9*H*-fluorene, 2FA

2-Bromo-9,9-dimethyl-9*H*-fluorene (1.1 g, 4.0 mmol), CuI (76 mg), $Pd(PPh_3)_2Cl_2$ (280 mg), and phenylacetylene (0.88 mL, 8.0 mmol) afforded **2FA** (0.80 g, 2.7 mmol) as a white solid that was purified by column chromatography on silica gel. Yield = 68%. ^{1}H NMR (CD_2Cl_2): δ 7.75 (m, 1H), 7.73 (d, J = 8.1 Hz, 1H), 7.64 (s, 1H), 7.57 (m, 1H), 7.56 (d, J = 2.4 Hz, 1H), 7.55 (dd, J = 11.8, 4.0 Hz, 1H), 7.47 (m, 1H), 7.37 (m, 5H), 1.51 (s, 6H, –CH_3). ^{13}C NMR (CD_2Cl_2): δ 154.42, 154.20, 139.93, 138.85, 131.89, 131.02, 128.85, 128.65, 128.17, 127.53, 126.35, 123.79, 123.11, 122.04, 120.67, 120.37, 90.53 (acetylene-*C*), 89.68 (acetylene-*C*), 47.25 (–*C*(CH_3)$_2$), 27.22 (–*C*H_3). Anal. calcd for $C_{23}H_{18}$: C, 93.84; H, 6.16. Found: C, 93.55; H, 5.80.

Data for 9,9-dimethyl-3-(phenylethynyl)-9*H*-fluorene, 3FA

3-Bromo-9,9-dimethyl-9*H*-fluorene (0.52 g, 1.9 mmol), CuI (36 mg), $Pd(PPh_3)_2Cl_2$ (130 mg), and phenylacetylene (0.42 mL, 3.8 mmol) afforded **3FA** (0.40 g, 1.4 mmol) as a pale yellow oil that was purified by column chromatography on silica gel. Yield = 72%. ^{1}H NMR (CD_2Cl_2): δ 7.97 (s, 1H), 7.80 (d, J = 8.2 Hz, 1H), 7.63 (d, J = 8.1 Hz, 2H), 7.56 (d, J = 7.9 Hz, 1H), 7.49 (t, J = 8.4 Hz, 2H), 7.41 (m, 5H), 1.53 (s, 6H, –CH_3). ^{13}C NMR (CD_2Cl_2): δ 154.41, 154.15, 139.94, 138.73, 131.97, 131.12, 128.88, 128.69, 128.20, 127.55, 123.81, 123.43, 123.19, 123.12, 122.18, 120.59, 90.25 (acetylene-*C*), 89.14 (acetylene-*C*), 47.36 (–*C*(CH_3)$_2$), 27.18 (–*C*H_3). Anal. calcd for $C_{23}H_{18}$: C, 93.84; H, 6.16. Found: C, 93.49; H, 5.90.

Data for 9,9-dimethyl-3-(phenylethynyl)-9*H*-fluorene, 4FA

4-Bromo-9,9-dimethyl-9*H*-fluorene (0.55 g, 2.0 mmol), CuI (38 mg), $Pd(PPh_3)_2Cl_2$ (140 mg), and phenylacetylene (0.44 mL, 4.0 mmol) afforded **4FA** (0.38 g, 1.3 mmol) as a pale yellow oil that was purified by column chromatography on silica gel. Yield = 65%. ^{1}H NMR (CD_2Cl_2): δ 8.67 (d, J = 8.8 Hz, 1H), 7.74 (d, J = 8.0 Hz, 2H), 7.58 (d, J = 8.0 Hz, 1H), 7.53 (d, J = 7.8 Hz, 1H), 7.47 (m, 6H), 7.36 (t, J = 7.6 Hz, 1H), 1.54 (s, 6H, –CH_3). ^{13}C NMR (CD_2Cl_2): δ 154.69, 154.43, 139.47, 139.13, 131.92, 131.72, 128.99, 128.94, 128.17, 127.42, 127.23, 123.77, 123.18, 123.15, 122.79, 116.77, 93.86 (acetylene-*C*), 88.95 (acetylene-*C*), 46.69 (–*C*(CH_3)$_2$), 27.29 (–*C*H_3). Anal. calcd for $C_{23}H_{18}$: C, 93.84; H, 6.16. Found: C, 93.51; H, 5.92.

Data for ((9,9-dimethyl-9*H*-fluoren-4-yl)ethynyl) trimethylsilane, 4FASi

4-Bromo-9,9-dimethyl-9*H*-fluorene (0.56 g, 1.9 mmol), CuI (37 mg), $Pd(PPh_3)_2Cl_2$ (135 mg), and ethynyltrimethylsilane (0.53 mL, 3.8 mmol) afforded **4FA** (0.19 g, 0.66 mmol) as a white solid that was purified by column chromatography on silica gel. Yield = 34%. ^{1}H NMR (CD_2Cl_2): δ 8.59 (t, J = 4.8 Hz, 1H), 7.49 (d, J = 8.2 Hz, 1H), 7.46 (dd, J = 7.8, 1.8 Hz, 2H), 7.39 (t, J = 7.8 Hz, 2H), 7.29 (t, J = 8.2 Hz, 1H), 1.48 (s, 6H, –CH_3), 0.40 (s, 9H, –Si(CH_3)$_3$). ^{13}C NMR (CD_2Cl_2): δ 154.64, 154.44, 139.68, 139.03, 131.95, 128.20, 127.18, 127.11, 123.38, 123.30, 122.72, 116.71, 104.56 (acetylene-*C*), 99.52 (acetylene-*C*), 46.58 (–*C*(CH_3)$_2$), 27.29 (–*C*H_3), 0.06 (–Si(*C*H_3)$_3$). Anal. calcd for $C_{20}H_{22}Si$: C, 82.70; H, 7.63. Found: C, 82.60; H, 7.55.

Synthesis of 4-ethynyl-9,9-dimethyl-9*H*-fluorene, 4FAH

K_2CO_3 (0.18 g, 1.3 mmol) was dissolved in methanol (7 mL) and added to a solution of **4FASi** (0.19 g, 0.66 mmol) in DCM (3 mL). After stirring for 2 h at 25 °C, the resulting mixture was treated with DCM (30 mL), and the organic layer was separated. The aqueous layer was further extracted with DCM (20 × 2 mL). The combined organic extracts were dried over $MgSO_4$, filtered, and evaporated to dryness to afford a white residue. The crude product was purified by washing with methanol (10 mL) to yield **4FAH** as a purple oil, 0.13 g (0.58 mmol). Yield = 88%. ^{1}H NMR (CD_2Cl_2): δ 8.58 (d, J = 8.0 Hz, m, 1H), 7.50 (dd, J = 4.7, 2.3 Hz, 3H), 7.41 (t, J = 4.8 Hz, 2H), 7.31 (t, J = 7.6 Hz, 1H), 3.59 (s, 1H, –CC*H*), 1.50 (s, 6H, –CH_3). ^{13}C NMR (CD_2Cl_2): δ 154.69, 154.39, 139.92, 138.85, 132.48, 128.29, 127.35, 127.14, 123.67, 123.21, 122.77, 115.60, 83.01 (acetylene-*C*), 82.15 (acetylene-*C*), 46.60 (–*C*(CH_3)$_2$), 27.27 (–*C*H_3). Anal. calcd for $C_{17}H_{14}$: C, 93.54; H, 6.46. Found: C, 93.24; H, 6.20.

General synthetic routes for *o*-carborane compounds (2FC, 3FC, 4FC, and 4FCH)

An excess amount of Et_2S (3.0 equivalent of an acetylene precursor) was added to a toluene solution (12 mL) of decaborane ($B_{10}H_{14}$, 1.3 equivalent per acetylene derivative) and acetylene precursors (**2FA**, **3FA**, **4FA**, and **4FAH**) at 298 K. After heating to reflux, the reaction mixture was further stirred for 24 h. The solvent was removed under vacuum. The crude product was purified by column chromatography on basic aluminum oxide (eluent: DCM/*n*-hexane (1/20, v/v)) and by washing with *n*-hexane (20 mL) to afford fluorene-based *o*-carborane compounds as a white solid.

Data for 2FC

Decaborane (0.16 g, 1.3 mmol), Et_2S (0.28 mL, 11 mmol), and **2FA** (0.29 g, 1.0 mmol) in toluene afforded **2FC** as a white solid. Recrystallization from a mixture of DCM/*n*-hexane afforded 0.17 g (0.40 mmol) of **2FC**. Yield = 40%. ^{1}H{^{11}B} NMR (CD_2Cl_2): δ 7.66 (s, 1H), 7.53 (s, 2H), 7.48 (d, J = 8.1 Hz, 2H), 7.39 (s, 2H), 7.33 (s, 2H), 7.19 (d, J = 7.9 Hz, 1H), 7.12 (t, J = 8.2 Hz, 2H), 3.37 (br s, 2H, CB-B*H*), 2.65 (br s, 2H, CB-B*H*), 2.57 (br s, 4H, CB-B*H*), 2.38 (br s, 2H, CB-B*H*), 1.29 (s, 6H, –CH_3). ^{13}C NMR (CD_2Cl_2): δ 154.61, 153.83, 141.52, 137.87, 131.10, 131.00, 130.71, 130.61, 129.56, 128.64, 127.55, 125.01, 123.08, 120.96, 119.96, 86.65 (CB–*C*), 86.04 (CB–*C*), 47.18 (–C(CH_3)$_2$), 26.86 (–*C*H_3). ^{11}B{^{1}H} NMR (CD_2Cl_2): δ −2.63 (br s, 2B), −9.18 (br s, 3B), −10.61 (br s,

5B). Anal. calcd for $C_{23}H_{28}B_{10}$: C, 66.96; H, 6.84. Found: C, 66.88; H, 6.70.

Data for 3FC

Decaborane (0.22 g, 1.8 mmol), Et_2S (0.39 mL, 3.6 mmol), and **3FA** (0.40 g, 1.4 mmol) in toluene afforded **3FC** as a white solid. Recrystallization from a mixture of DCM/*n*-hexane afforded 0.21 g (0.52 mmol) of **3FC**. Yield = 38%. $^1H\{^{11}B\}$ NMR (CD_2Cl_2): δ 7.79 (s, 1H), 7.68 (d, J = 6.0 Hz, 1H), 7.51 (d, J = 7.8 Hz, 2H), 7.41 (d, J = 7.2 Hz, 2H), 7.34 (t, J = 3.6 Hz, 2H), 7.21 (d, J = 8.2 Hz, 2H), 7.14 (t, J = 7.3 Hz, 2H), 3.40 (br s, 2H, CB-B*H*), 2.57 (br s, 6H, CB-B*H*), 2.37 (br s, 2H, CB-B*H*), 1.36 (s, 6H, –CH_3). ^{13}C NMR (CD_2Cl_2): δ 156.16, 154.08, 139.87, 138.15, 131.08, 130.98, 130.63, 130.17, 129.88, 128.64, 128.41, 127.51, 123.10, 122.72, 122.67, 120.47, 86.39 (CB–*C*), 85.99 (CB–*C*), 47.04 (–*C*$(CH_3)_2$), 26.87 (–*C*H_3). $^{11}B\{^1H\}$ NMR (CD_2Cl_2): δ −2.66 (br s, 2B), −9.11 (br s, 3B), −10.56 (br s, 3B), −11.07 (br s, 2B). Anal. calcd for $C_{23}H_{28}B_{10}$: C, 66.96; H, 6.84. Found: C, 66.80; H, 6.69.

Data for 4FC

Decaborane (0.21 g, 1.7 mmol), Et_2S (0.37 mL, 3.4 mmol), and **4FA** (0.38 g, 1.3 mmol) in toluene afforded **4FC** as a white solid. Recrystallization from a mixture of EA/*n*-hexane afforded 0.06 g (0.14 mmol) of **4FC**. Yield = 11%. $^1H\{^{11}B\}$ NMR (CD_2Cl_2): δ 8.67 (d, J = 8.0 Hz, 1H), 7.78 (d, J = 8.1 Hz, 1H), 7.43 (d, J = 6.4 Hz, 1H), 7.38 (t, 7.4 Hz, 2H), 7.28 (d, J = 7.3 Hz, 1H), 7.21 (d, J = 7.8 Hz, 2H), 7.11 (q, J = 8.2 Hz, 2H), 6.96 (t, J = 7.8 Hz, 2H), 3.66 (br s, 2H, CB-B*H*), 2.98 (br s, 2H, CB-B*H*), 2.58 (br s, 2H, CB-B*H*), 2.48 (br s, 2H, CB-B*H*), 1.25 (s, 6H, –CH_3). ^{13}C NMR (CD_2Cl_2): δ 157.22, 154.92, 140.38, 137.66, 135.28, 131.12, 130.68, 130.36, 129.04, 128.30, 128.23, 126.84, 126.58, 126.17, 125.03, 122.72, 90.39 (CB–*C*), 89.85 (CB–*C*), 46.00 (–*C*$(CH_3)_2$), 27.67 (–*C*H_3). $^{11}B\{^1H\}$ NMR (CD_2Cl_2): δ −2.61 (br s, 1B), −3.65 (br s, 1B), −9.97 (br s, 3B), −11.26 (br s, 5B). Anal. calcd for $C_{23}H_{28}B_{10}$: C, 66.96; H, 6.84. Found: C, 66.75; H, 6.68.

Data for 4FCH

Decaborane (92 mg, 0.75 mmol), Et_2S (0.19 mL, 1.7 mmol), and **4FAH** (0.13 g, 0.58 mmol) in toluene afforded **4FCH** as a white solid. Recrystallization from a mixture of acetone/MeOH afforded 19 mg (55 μmol) of **4FCH**. Yield = 10%. $^1H\{^{11}B\}$ NMR (CD_2Cl_2): δ 8.21 (d, J = 7.5 Hz, 1H), 7.72 (d, J = 8.0 Hz, 1H), 7.52 (d, J = 7.3 Hz, 2H), 7.36 (m, 2H), 7.32 (t, J = 8.2 Hz, 1H), 4.98 (s, 1H, CB-C*H*), 2.86 (br s, 2H, CB-B*H*), 2.74 (br s, 2H, CB-B*H*), 2.34 (br s, 6H, CB-B*H*), 1.44 (s, 6H, –CH_3). ^{13}C NMR (CD_2Cl_2): δ 157.60, 155.29, 137.07, 135.80, 131.02, 130.28, 128.51, 127.66, 127.21, 125.71, 124.71, 123.70, 78.44 (CB–*C*), 60.41 (CB–*C*), 46.22 (–*C*$(CH_3)_2$), 28.02 (–*C*H_3). $^{11}B\{^1H\}$ NMR (CD_2Cl_2): δ −4.23 (br s, 3B), −9.89 (br s, 3B), −11.15 (br s, 2B), −14.31 (br s, 2B). Anal. Calcd for $C_{17}H_{24}B_{10}$: C, 60.68; H, 7.19. Found: C, 60.55; H, 7.10.

Synthesis of *nido*-4FC, (*nido*-from of 4FC)·(NBu_4)

4FC (18 mg, 43 μmol) was dissolved in 0.17 mL of a 1.0 M THF solution of *n*-tetrabutylammonium fluoride (TBAF) at 25 °C. The reaction mixture was heated to reflux (60 °C) and stirred for 24 h. After cooling to 25 °C, the resulting mixture was treated with 10 mL of distilled water and 10 mL of DCM, and the organic portion was then separated. The aqueous layer was further extracted with DCM (10 mL). The combined organic portions were dried over $MgSO_4$, filtered, and concentrated to dryness, thereby affording a pale-yellow residue. The crude product upon washing with methanol (15 mL) afforded *nido*-**4FC** as a white solid (15 mg, Yield = 54%). $^1H\{^{11}B\}$ NMR (CD_2Cl_2): δ 8.37 (d, J = 7.7 Hz, 1H), 7.50 (dd, J = 5.6, 2.5 Hz, 1H), 7.42 (t, J = 8.8 Hz, 1H), 7.25 (s, 2H), 7.06 (d, J = 6.3 Hz, 4H), 6.62 (t, J = 7.1 Hz, 1H), 6.52 (t, J = 7.5 Hz, 2H), 3.03 (m, 8H, *n*-butyl-CH_2), 2.80 (br s, 1H, CB-B*H*), 2.63 (br s, 1H, CB-B*H*), 2.18 (br s, 1H, CB-B*H*), 1.94 (br s, 1H, CB-B*H*), 1.62 (br s, 5H, CB-B*H*), 1.56 (m, 8H, *n*-butyl-CH_2), 1.37 (m, 8H, *n*-butyl-CH_2), 1.33 (s, 6H, –CH_3), 0.98 (t, J = 9.8 Hz, 12H, *n*-butyl-CH_3), −2.18 (s, 1H, B–*H*–B). ^{13}C NMR (CD_2Cl_2): δ 154.00, 153.80, 140.25, 140.11, 139.58, 137.29, 131.47, 131.03, 126.74, 126.34, 126.08, 126.04, 126.00, 125.15, 121.68, 120.28, 59.31 (*n*-butyl-*C*H_2), 45.70 (–*C*$(CH_3)_2$), 28.46 (–*C*H_3), 26.79, 24.23 (*n*-buthyl-*C*H_2), 20.02 (*n*-butyl-*C*H_2), 13.73 (*n*-butyl-*C*H_3). $^{11}B\{^1H\}$ NMR (CD_2Cl_2): δ −8.35 (br s, 1B), −11.82 (br s, 1B), −12.98 (br s, 1B), −14.76 (br s, 1B), −16.82 (br s, 1B), −19.07 (br s, 1B), −20.38 (br s, 1B), −32.58 (br s, 1B), −35.38 (br s, 1B). Anal. calcd for $C_{39}H_{64}B_9N$: C, 72.71; H, 10.01; N, 2.17. Found: C, 72.50; H, 9.99; N, 2.12.

X-ray crystallography

Single X-ray quality **2FC**, **3FC**, **4FC**, and **4FCH** crystals were grown for X-ray diffractometry from DCM/*n*-hexane (for **2FC** and **3FC**), EA/*n*-hexane (for **4FC**), and acetone/MeOH (for **4FCH**) mixtures. Each single crystal was coated with Paratone oil and mounted on a glass capillary. Crystallographic measurements were performed using a Bruker D8QUEST CCD area detector diffractometer with graphite monochromated Mo-Kα radiation (λ = 0.71073 Å). The structures of the *o*-carboranyl compounds were assessed using direct methods, and all nonhydrogen atoms were subjected to anisotropic refinement with the full-matrix least-squares method on F^2 using a SHELXTL/PC software package. X-ray crystallographic data are available in the CIF format (CCDC 2057685 for **2FC**, 2057686 for **3FC**, 2057688 for **4FC**, and 2057687 for **4FCH**, respectively), and they are provided free of charge by the CCDC.† Hydrogen atoms were placed at their geometrically calculated positions and refined using a riding model on the corresponding carbon atoms with isotropic thermal parameters. Detailed crystallographic data and selected bond lengths and angles are provided in Tables S1 and S2 in the ESI.†

UV-vis absorption and photoluminescence (PL) measurements

UV-vis absorption and PL spectra of all *o*-carboranyl compounds were acquired using V-530 (Jasco) and Fluoromax-4P (HORIBA) spectrophotometers, respectively. UV-vis absorption and PL measurements for the solutions were performed at 298 K in oxygen-free and anhydrous THF with a 1 cm quartz cuvette (3.0×10^{-5} M). Furthermore, PL measurements were performed

under various conditions, including different oxygen-free solvents (toluene, DCM, and THF/distilled water mixtures; 3.0 $\times$ 10^{-5} M) in the THF solution (3.0 $\times$ 10^{-5} M) at 77 K, and as a film at 298 K. Thin films of the *o*-carborane compounds in PMMA were obtained by spin coating a THF solution (1 mL) of PMMA (50 mg) containing each *o*-carborane compound (5 wt% *versus* PMMA) on a 10 mm $\times$ 10 mm quartz plate (thickness = 1 mm). The absolute photoluminescence quantum yields (PLQYs) in the THF solution (3.0 $\times$ 10^{-5} M) and in the film were obtained at 298 K using a Fluoromax-4P spectrophotometer (HORIBA) equipped with a 3.2-inch integrating sphere (FM-sphere, HORIBA). Fluorescence decay lifetimes and transient PL spectra were measured using a time-correlated single-photon counting spectrometer (FLS920-EDINBURGH instrument at the Central Laboratory of Kangwon National University) equipped with an EPL-375 ps pulsed semiconductor diode laser excitation source and a microchannel plate photomultiplier tube (MCP-PMT, 200–850 nm) detector.

Computational calculation studies

The geometries of the *o*-carboranyl compounds **2FC**, **3FC**, and **4FC** in their ground (S_0) and first-excited (S_1) states in THF were optimized at the PBE0/6-31G(d,p)[74] level of theory. Vertical excitation energies in the optimized S_0 and S_1 state geometries were calculated using the TD-DFT method[75] at the same level of theory. The solvent effects were evaluated using a self-consistent reaction field method based on the integral equation formalism of the polarizable continuum model with THF as the solvent.[76] Most stable geometries were determined by constructing one-dimensional potential energy surfaces as a function of each dihedral angle (Ψ) by rotating the *o*-carborane cage between approximately −180° and 180° at intervals of 30° to yield 18 initial conformations for each compound. Conformations that exhibited physically impossible atomic overlaps were excluded from further geometric optimizations. The dihedral angle was fixed while other geometric variables were fully relaxed for the geometry optimization and energy calculations of the resulting initial conformations using the Gaussian 16 software program.[77] The contribution (%) of a group in a molecule for each molecular orbital was calculated using the GaussSum 3.0 software program.[78]

Results and discussion

Synthesis and characterization

Synthetic protocols for **2FC**, **3FC**, and **4FC** with *o*-carborane cages appended at the C2-, C3-, and C4-positions of each fluorene moiety, respectively, are provided in Scheme 1. To investigate the structural and electronic effects of *o*-carborane on the photophysical characteristics, corresponding derivatives for **4FC**, **4FCH** (structure without the terminal phenyl ring from **4FC**), and *nido*-**4FC** (= [*nido*-form of **4FC**]·[NBu_4]) were synthesized (Scheme 1).

Sonogashira couplings between phenylacetylene and either 2-, 3-, or 4-bromo-9,9-dimethyl-9*H*-fluorene afforded **2FA**, **3FA**, and **4FA**, respectively, in high yields (68, 72, and 65%, respectively). The acetylene precursor **4FAH** was prepared by the Sonogashira reaction of 4-bromo-9,9-dimethyl-9*H*-fluorene with ethynyltrimethylsilane, followed by treatment with a mild base (K_2CO_3) to deprotect the trimethylsilyl group. The cage-forming reaction[79–81] of decaborane ($B_{10}H_{14}$) with each acetylene precursor (**2FA**, **3FA**, **4FA**, and **4FAH**) afforded *o*-carborane compounds **2FC**, **3FC**, **4FC**, and **4FCH**, respectively, in relatively low yields (10–40%, Scheme 1). In particular, the cage-forming reaction was difficult for **4FC** and **4FCH** because of the steric hindrance of the bulky fluorene moiety that leads to significantly low yields (~10%). Subsequent treatments using **4FC** with excess amounts of a weak base like *n*-tetrabutylammonium fluoride (NBu_4F, TBAF) led to the conversion of the *closo*-carborane species to the *nido*-species, *i.e.*, *nido*-**4FC** (= [*nido*-form of **4FC**]·[NBu_4]) with a moderate yield (54%).

All acetylene precursors and fluorene-based *o*-carboranyl compounds were characterized using multinuclear nuclear magnetic resonance (NMR) spectroscopy (Fig. S1–S15 in the ESI†) and elemental analyses. The $^1H\{^{11}B$ decoupled$\}$ spectra of the *closo*-*o*-carboranyl compounds exhibited expected resonances that can be assigned to the fluorene group, dimethyl

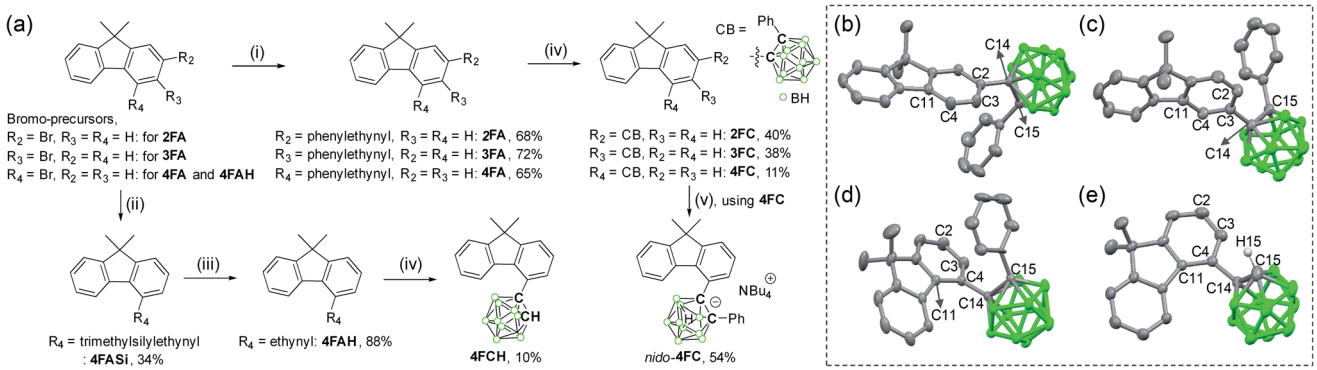

Scheme 1 Synthetic routes for the fluorene based *o*-carboranyl compounds. Reagents and conditions: (i) phenylacetylene, CuI, $Pd(PPh_3)_2Cl_2$, NEt_3/toluene, 110 °C, 24 h. (ii) Ethynyltrimethylsilane, CuI, $Pd(PPh_3)_2Cl_2$, NEt_3/toluene, 110 °C, 24 h. (iii) K_2CO_3, MeOH/DCM, 25 °C, 2 h. (iv) $B_{10}H_{14}$, Et_2S, toluene, 120 °C, 24 h. (v) TBAF, THF, 60 °C, 24 h. The figures in the box show the molecular structures of (b) **2FC**, (c) **3FC**, (d) **4FC**, and (e) **4FCH** (50% thermal ellipsoids, solvent molecules in unit cell and H atoms were omitted for clarity).

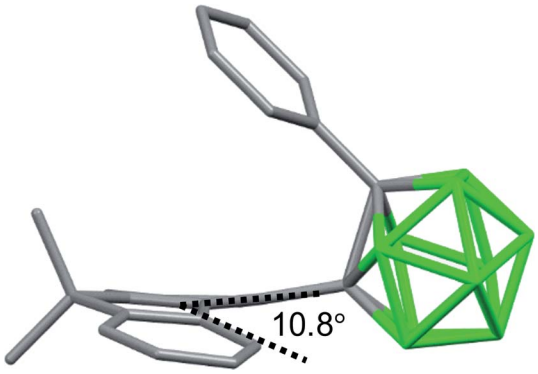

Fig. 1 Molecular structure of **4FC** exhibiting a distorted fluorene plane formation.

groups, terminal aryl rings (for **2FC**, **3FC**, and **4FC**), and the C*H* of *o*-carborane (for **4FCH**). The broad $^{1}H\{^{11}B\}$ peaks present in the upfield region (−2.18 ppm) of the *nido*-**4FC** spectrum are characteristic of the B–*H*–B bridge protons of *nido*-*o*-carboranyl cages. Furthermore, observations of three or four broad peaks between −2 and −15 ppm in the $^{11}B\{^{1}H\}$ NMR spectra of **2FC**, **3FC**, **4FC**, and **4FCH** confirm the presence of a *closo*-*o*-carborane cage. Moreover, the $^{11}B\{^{1}H\}$ NMR spectra of *nido*-**4FC** and *nido*-**CB2** showed nine broad peaks between −8 and −36 ppm; these signals were significantly shifted to the upfield region because of the anionic character of the *nido*-*o*-carborane structure, which clearly indicates the presence of the *nido*-*o*-carborane cage.

The X-ray diffraction analysis results for **2FC**, **3FC**, and **4FC** demonstrate their solid-state molecular structures (Scheme 1b–d, respectively). Detailed parameters, including the selected bond length and angles, are listed in Tables S1 and S2.† The fluorene group appended to the *o*-carborane cage in **4FC** was significantly distorted, wherein the angle between the two phenyl rings was 10.8° (Fig. 1) and the fluorene plane of both **2FC** and **3FC** exhibited perfect planarity. These structural features were attributed to the severe steric hindrance around the carborane cage in **4FC**, which implies that structural variation centered at the cage was considerably restricted.

Photophysical analysis for *o*-carboranyl compounds with theoretical calculations

To investigate the photophysical properties of the fluorene-based *o*-carboranyl compounds, ultraviolet-visible (UV-vis) absorption and photoluminescence (PL) spectroscopy were performed under various conditions (Fig. 2 for **2FC**, **3FC**, **4FC**, and *nido*-**4FC**, Fig. S16† for **4FCH**, and Table 1). The major lowest-absorption bands centered at λ_{abs} = 302–318 nm for the *closo*-*o*-carboranyl compounds in THF were attributed to vibronic structures undergoing spin-allowed π–π* transitions on the fluorene moiety. 9,9-Dimethyl-9*H*-fluorene exhibited similar strong absorption peaks in this region (Fig. S17,† λ_{abs} = 302 nm (ε = 6700 M^{-1} cm^{-1}) and 291 nm (4440 M^{-1} cm^{-1})). Specific features of the low-energy absorption for these *closo*-compounds include substantially tailing absorption bands at 350 nm and broad absorption features attributed to typical ICT transitions in the *o*-carborane cages. These ICT characteristics for *closo*-compounds were verified by the fact that low-energy absorption bands were not observed in the spectrum of 9,9-dimethyl-9*H*-fluorene (Fig. S17†). Furthermore, *nido*-**4FC** did not exhibit low-absorption spectra in the region 310–350 nm (Fig. 2c, black dash-line), which strongly indicates that the anionic feature of *nido*-*o*-carborane can inhibit ICT transition, wherein *o*-carborane acts as an electronic acceptor. The UV-vis spectral properties are highly consistent with the theoretical calculations (*vide infra*).

The origin of electronic transitions in **2FC**, **3FC**, and **4FC** were determined using time-dependent density functional theory (TD-DFT) calculations.[75] Ground (S_0) and first-excited (S_1) states of the compounds were optimized at the PBE0/6-31G(d) level of theory (Fig. 3). Each calculated structure of *closo*-compounds is based on its X-ray crystal structure (Scheme 1b–d). An integral equation formalism of the polarizable continuum model (IEFPCM) is employed to consider the THF solvent effect.[76] S_0 state calculations indicate that the lowest-energy electronic transitions for these compounds are associated with transitions from the HOMO to the LUMO (Fig. 3). The HOMO of each compound is predominantly localized on the fluorene moiety (>96% in all *closo*-compounds, Tables S4, S6, and S8†); however, the LUMOs are substantially distributed over

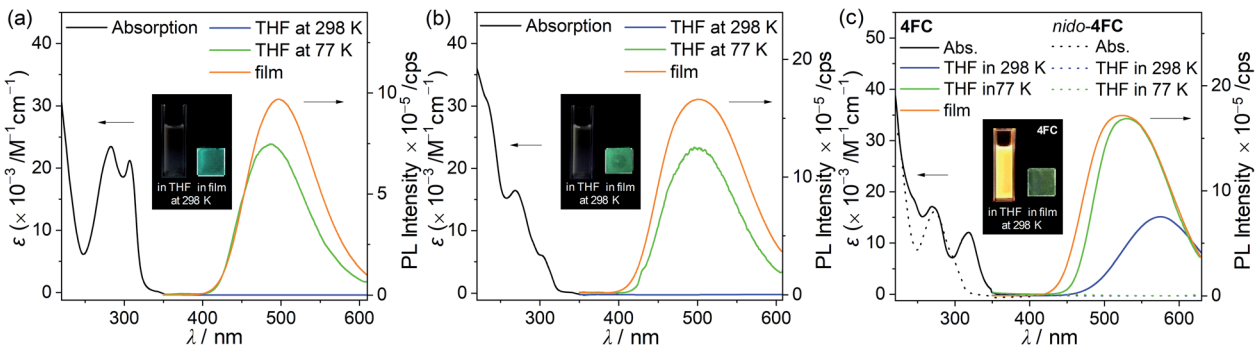

Fig. 2 UV-vis absorption (left side) and PL spectra (right side) for (a) **2FC** (λ_{ex} = 307 nm), (b) **3FC** (λ_{ex} = 300 nm), (c) **4FC** and *nido*-**4FC** (λ_{ex} = 318 nm). Black line: absorption spectra in THF (3.0 × 10^{-5} M); blue line: PL spectra in THF (3.0 × 10^{-5} M) at 298 K; green line: PL spectra in THF (3.0 × 10^{-5} M) at 77 K; and orange line: PL spectra in film (5 wt% doped with PMMA) at 298 K. Inset figures show the emission color in each state under irradiation by a hand-held UV lamp (λ_{ex} = 265 nm).

Table 1 Photophysical data for fluorene-based *o*-carboranyl compounds (**2FC**, **3FC**, **4FC**, *nido*-**4FC**, and **4FCH**)

			λ_{em}/nm						Φ_{em}[e]			τ_{obs}/ns		k_r[f]/$\times 10^7$ s^{-1}		k_{nr}[g]/$\times 10^8$ s^{-1}	
	λ_{abs}[a]/nm ($\varepsilon \times 10^{-3}$ M^{-1} cm^{-1})	λ_{ex}/nm	Tol[b]	THF[b]	DCM[b]	77 K[a]	Film[c]	f_w = 90%[b,d]	THF[b]	Film[c]	f_w = 90%[b,d]	THF[b]	Film[c]	THF	Film	THF	Film
2FC	307 (21.2), 283 (23.5)	307	—[h]	—[h]	—[h]	486	498	503	<0.01	0.29	0.26	—[h]	4.6	—	6.3	—	1.5
3FC	302 (6.1), 268 (16.4)	302	—[h]	—[h]	—[h]	498	500	515	<0.01	0.24	0.19	—[h]	4.1	—	5.8	—	1.8
4FC	318 (12.1), 269 (17.1)	318	553	577	596	528	523	536	0.05	0.42	0.36	2.1	3.9	2.4	10.8	4.6	1.6
nido-**4FC**	271 (16.1)	300	—[h]	—[h]	—[h]	—[h]	—[h]	—	—	—	—	—	—	—	—	—	—
4FCH	309 (8.1), 271 (10.9)	309	356, 546	356, 579	356, 586	340, 527	—	—	0.01 (CT)	0.04 (CT)	—	-[h]	7.6	—	0.53	—	1.3

[a] 3.0×10^{-5} M in oxygen-free and anhydrous THF. [b] $c = 3.0 \times 10^{-5}$ M in oxygen-free and anhydrous solvent, observed at 298 K. [c] Measured in the film state (5 wt% doped in PMMA). [d] Water fraction in a THF–water mixture. [e] Absolute PL quantum yield. [f] $k_r = \Phi_{em}/\tau_{obs}$. [g] $k_{nr} = k_r(1/\Phi_{em} - 1)$. [h] Not observed because of weak emission.

the *o*-carborane units (>30% in all compounds). These calculation results for S_0 states suggest that the low-energy electronic transitions of *o*-carboranyl-fluorene compounds originate from both local π–π* transitions on the fluorene group and substantial ICT transitions involving *o*-carborane cages.

The emissive features of *o*-carboranyl compounds were examined by PL measurements (Fig. 2 and Table 1). While the PL spectra of **4FC** in THF at 298 K exhibited significant emission in the region centered at $\lambda_{em} = 577$ nm (orange emission, inset of Fig. 2c), **2FC** and **3FC** hardly showed any emissive pattern. Because the PL spectra for **4FC** was red-shifted upon increasing solvent polarities (positive solvatochromic effect, $\lambda_{em} = 553$ nm in toluene to 596 nm in dichloromethane, $\Delta\lambda_{em} = 43$ nm, Table 1 and Fig. S18a†), it strongly indicated that the emissive band is attributed to the ICT characteristic. Furthermore, computational results for the S_1 states of *o*-carboranyl compounds supported this observation. Emissions for compounds are dominated by HOMO → LUMO transitions (Fig. 3). The HOMOs are significantly localized on the fluorene moiety (>93% in all compounds, Tables S4, S6, and S8†), whereas the LUMOs are centered on the *o*-carborane units (>83%). This suggests that emissions originate from ICT processes between the *o*-carborane and fluorene groups.

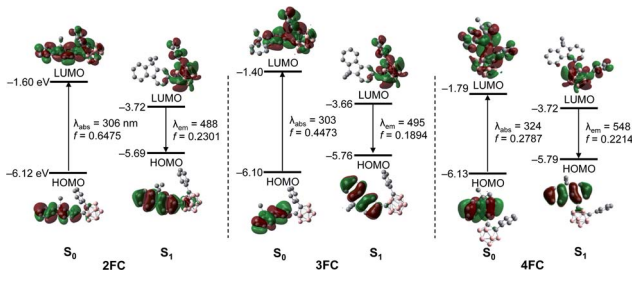

Fig. 3 Frontier molecular orbitals for **2FC**, **3FC**, and **4FC** in their ground state (S_0) and first excited singlet state (S_1) with relative energies obtained from DFT calculations (isovalue 0.04). Transition energy (in nm) was calculated using the TD-PBE0 method with 6-31G(d) basis sets.

Interestingly, these three *o*-carboranyl compounds demonstrated intense emission at $\lambda_{em} = 486$–528 nm (Fig. 2 and Table 1) in the rigid state (THF at 77 K and film (5 wt% doped in PMMA)), which can be attributed to ICT-based emission. These features result from the restricted elongation of the C–C bond of the *o*-carborane triggered by excitation, which prevents radiative decay based on ICT transitions.[62–64] The optimized structures of *closo*-compounds based on their S_0 and S_1 states demonstrate C–C bond fluctuations (Table 2). The bond lengths of *o*-carborane cages in the S_1 state were 2.39–2.48 Å; these were considerably larger than those in the S_0 states (1.67–1.83 Å) and the experimentally measured values (~1.73 Å) for compounds based on their X-ray structures. Consequently, all the

Table 2 C–C bond lengths in the *o*-carborane cages (Å) of **2FC**, **3FC**, and **4CB** and the dihedral angles (Ψ/°) between the C–C bonds of the *o*-carborane cages (labelled C14–C15 in X-ray crystal structures) and fluorene planes

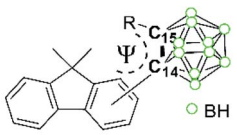

R = Ph for **2FC**, **3FC**, and **4FC**
= H for **4FCH**

	C–C bond/Å			Ψ/°		
		Calc.[b]			Calc.[b]	
	Exp.[a]	S_0	S_1	Exp.[a]	S_0	S_1
2FC	1.75	1.78	2.46	87.1	87.9	0.0
3FC	1.73	1.77	2.44	82.9	88.3	1.8
4FC	1.76	1.83	2.48	89.3	87.9	0.1
4FCH	1.72	1.67	2.39	82.7	87.0	1.6

[a] Experimental values calculated from their X-ray crystal structures. [b] Calculated values from their ground state (S_0) and first excited singlet state (S_1) optimized structures.

compounds revealed that absolute quantum yields (a_{em} = 29% for **2FC**, 24% for **3FC**, and 42% for **4FC**, Table 1) in the film were dramatically enhanced compared with those (<1% for **2FC** and **3FC**, and 5% for **4FC**) in THF at 298 K. In particular, the additional reason for the enhanced emission of three compounds in the film (solid) state was investigated based on further PL measurements in a THF–water mixture (3.0×10^{-5} M, Fig. S19†). The low-energy emission around 500–550 nm was drastically enhanced by an increased water fraction (f_w). Consequently, each maximized aggregation state in THF/water (f_w = 90%) for the compounds was associated with intense greenish emission patterns (λ_{em} = 503–536 nm) and high Φ_{em} values (26%, 19%, and 36% for **2FC**, **3FC**, and **4FC**, respectively; Table 1) similar to those observed in the film state. These observations are characteristic of aggregation induced emission (AIE) phenomena.

Nido-**4FC** did not present any emissive traces in THF at 298 K and 77 K (Fig. 2c and Table 1); totally differed from the features of *closo*-compounds, which strongly suggests that the ICT process can be obstructed by the anionic characteristic of *nido*-*o*-carborane. This observation paradoxically reveals that all emissive characteristics of *closo*-compounds are significantly correlated with the ICT transition involving *closo*-*o*-carborane.

Interestingly, **4FCH** exhibited a significantly weak dual-emissive trace centered at e_{em} = 356 and 579 nm in the THF at 298 K; however, the emissive pattern was distinctly observed in the rigid state (THF at 77 K and film state, Fig. S16† and Table 1). Based on the PL spectra of 9,9-dimethyl-9*H*-fluorene in THF at 298 K that exhibits an emission centered at e_{em} = 341 nm (Fig. S17†) and a red-shifted emission in the region of 500–600 nm (positive solvatochromic effect, λ_{em} = 546 nm in toluene to 586 nm in dichloromethane, $\Delta\lambda_{em}$ = 40 nm; Table 1 and Fig. S18b†), high- and low-energy regions predominantly originate from π–π* locally excited (LE) transitions on the fluorene group and ICT transitions between the *o*-carborane cage and fluorene moiety, respectively. This leads to LE- and ICT-based emissions. Furthermore, high-energy emissions of **4FCH** remain unchanged in solvents with different polarities, which strongly indicates LE-characteristics. Consequently, the revelation of LE-based emission leads to a drastic decrease in the efficiency of ICT-based emissions (Φ_{em} = 1% in THF at 298 K and 4% in film state, Table 1) because excitons on **4FCH** are separated into both LE and ICT transitions.

Such different optical behaviors between **4FC** and other *closo*-compounds were exhibited moderately by only **4FC** during the ICT-based emission (Φ_{em} = 5%) in THF at 298 K. This suggests that the ICT-based radiative-decay process based on *o*-carboranyl compounds is severely affected by structural motion. As shown in the structural feature of **4FC** (Scheme 1d), the fluorene plane is distorted significantly by intramolecular steric hindrance, and the rotation of the *o*-carborane cage in **4FC** is definitely restricted. However, the *o*-carboranes of other *closo*-compounds can be freely rotated. Indeed, the intensity of the Raman spectra of **4FC** was much weaker than those of **2FC** and **3FC** (Fig. S20†), indicating that the structural motion of **4FC** is effectively restricted compared to those for **2FC** and **3FC**. Furthermore, such a restriction of rotational motion for **4FC** differs from that for **2FC**, **3FC**, and **4FCH**, and it can be revealed by the energy calculation results of their S_0 states upon changing the dihedral angles associated with their *o*-carboranyl cages (Fig. 5, *vide infra*). Consequently, the structural fluctuations around the *o*-carborane cage can decrease the efficiency of ICT-based radiative decay for **2FC** and **3FC**, and it can further reinforce LE-based emission instead of the ICT process.

Comparative analysis of the ICT-based radiative decay of *o*-carboranyl compounds in the solid state

To analyze and compare the efficiency of the ICT-based emission from each *closo*-*o*-carboranyl compound in the film (solid), radiative (k_r) and nonradiative (k_{nr}) decay constants were estimated using Φ_{em} and emission decay lifetimes (τ_{obs}) (Table 1). The τ_{obs} values for all *closo*-compounds determined at 298 K were found to be similar on the nanosecond time scale (1.3–4.3 ns, Fig. 4 for **4FC**; Fig. S21† for **2FC**, **3FC**, and **4FCH**; and Table 1), which demonstrated their fluorescent nature. The k_r value calculated using the Φ_{em} and τ_{obs} of **4FC** in the film was

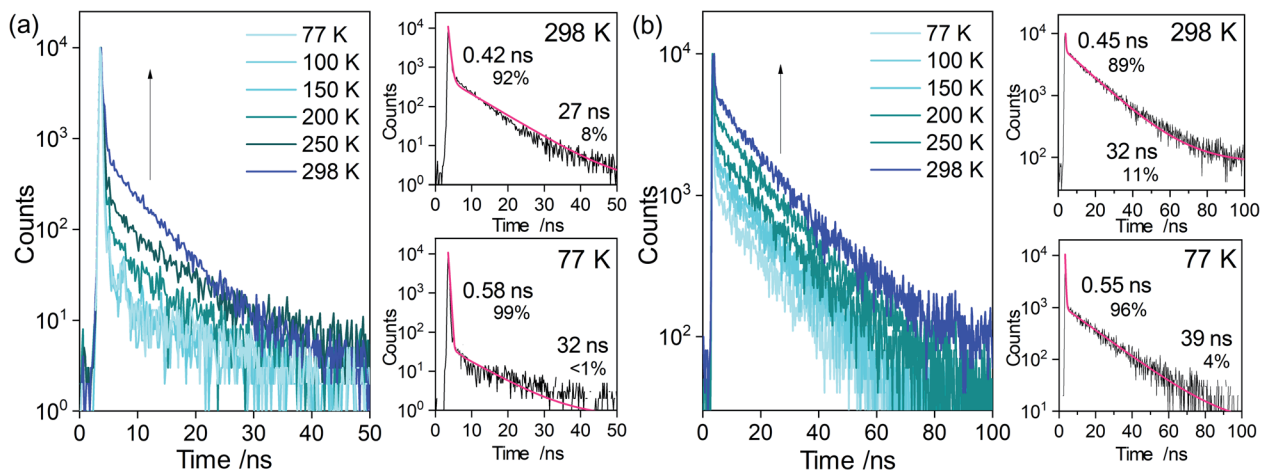

Fig. 4 Transient PL decay profiles for **4FC** (a) in oxygen-free and anhydrous THF (3.0×10^{-5} M) detected at 528 nm and (b) in the film state (5 wt% doped in PMMA) detected at 523 nm based on changes in temperature. Each red line represents its double exponential fitting curve.

estimated to be 1.1×10^8 s^{-1} (Table 1). This was approximately two times more than those for **2FC** (6.3×10^7 s^{-1}) and **3FC** (5.8×10^7 s^{-1}), and 20 times larger than that of **4FCH** (5.3×10^6 s^{-1}). Furthermore, the k_{nr} (1.6×10^8 s^{-1}) of **4FC** was similar to those of other compounds (1.5×10^8 s^{-1} for **2FC**, 1.8×10^8 s^{-1} for **3FC**, and 1.3×10^8 s^{-1} for **4FCH**). Quantitative results for the ICT-based emission strongly suggest that the structural formation around *o*-carborane cages is determined by structural rigidity and has a significant relevance to the efficiency of radiative decay based on ICT transitions. Furthermore, this can lead to the enhancement of ICT-based emissions.

The calculated relative energy of each *closo-o*-carboranyl compound in its ground state (S_0, black solid-dot line in Fig. 5) demonstrated the structural environment around the *o*-carborane cage. These results were calculated as functions of dihedral angles (Ψ = from −180° to 180° range in 30° steps) between the fluorene plane and the C–C bond of *o*-carborane (Table 2) using the PBE0 functional and 6-31G(d) basis set.

The relative energy of each compound was presented against the thermodynamic energy of each S_0-optimized structure in THF (energy for each S_0-optimized state = 0 eV). The Ψ values of the S_0-optimized structure for the *closo*-compounds were estimated to be ~88°, which closely reflected the experimental values for compounds, obtained by X-ray diffraction analyses (82.7–87.1°, Table 2). Meanwhile, values for the S_0-optimized state indicated that the C–C bond of the *o*-carborane became parallel to the fluorene plane (Ψ = 0.0–1.8°). These results strongly suggest that the rotation motion of *o*-carborane cages for all *closo*-compounds can occur during the radiative excitation and relaxation processes. Furthermore, the relative energy barrier on the S_0-states for **2FC**, **3FC**, and **4FCH** did not exceed 0.18 eV throughout the entire Ψ range (Fig. 5), while the lowest energy points of **4FC** were observed around Ψ = 90 and −90°; moreover, the energy maximum point was ~0.95 eV (Ψ = 120°).

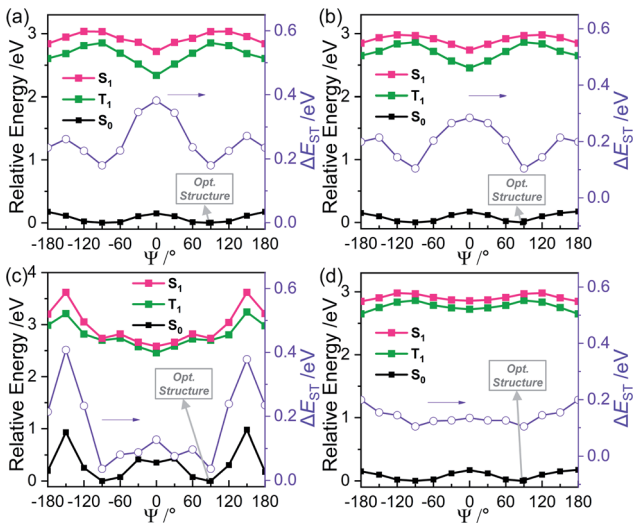

Fig. 5 Relative energy diagrams of S_0, S_1, and T_1 states for (a) **2FC**, (b) **3FC**, (c) **4FC**, and (d) **4FCH** on changing the dihedral angle (Ψ). Each purple line indicates the energy gap between the relative energy for the S_1 and T_1 states.

Considering the thermal energy value at 298 K = 0.59 kcal mol^{-1} (~0.025 eV mol^{-1})—calculated as k_BT (k_B = Boltzmann constant, 1.98 cal K^{-1} mol^{-1})—the features indicate that the structural formation of **4FC** was fixed at $\Psi \approx 90°$ in all states, whereas *o*-carborane cages in **2FC**, **3FC**, and **4FCH** can be freely rotated in the solution state at ambient temperature and can further exist in various structural forms in the solid state. Consequently, calculation and experimental results confirmed that the structural rigidity of **4FC** led to efficient radiative decay based on ICT transitions associated with *o*-carborane.

TADF characteristics revealed by the rigid structural formation

When investigating the radiative decay lifetime of **4FC**, a decay feature was observed, wherein exponential components are separated as prompt and delayed decay profiles. In particular, transient PL decay for the ICT-based emission of **4FC** in THF at 298 K revealed that PL decay curves are best fitted with short-lived (τ_{obs} = 0.42 ns, Fig. 4a) and comparatively long-lived (27 ns) decay components, respectively. Furthermore, PL spectral profiles of **4FC** in aerated THF at 298 K exhibited slightly lower intensities (Fig. S22†) compared to that in oxygen-free THF (the PL in Fig. 2c); this indicates that the oxygen-sensitive radiative decay component related to the triplet (T_1) excited state is slightly involved with the ICT-based emission of **4FC**. These results suggest that long-lived emissions can be assigned to the delayed fluorescence that arises from the S_1 state through upconversion from the T_1 state; *i.e.*, from the reverse intersystem crossing.

Furthermore, the intensity of the delayed component (~30 ns) gradually decreases as the temperature is decreased from 298 K to 77 K (8% at 298 K to <1% at 77 K, Fig. 4a, inset); this confirms that the delayed emission can be assigned to TADF. In addition, the delayed fluorescence was found to be more intensely observed in the film (solid) state than in solution. Indeed, transient PL decays of **4FC** in the film demonstrated a greater portion (4–11%, Fig. 4b) of the delayed component (32–39 ns) than that of the prompt component. Temperature-dependent PL decay profiles in the film state verified the TADF characteristic of the delayed emission. Furthermore, the PL decay profiles of the other *closo-o*-carboranyl compounds **2FC**, **3FC**, and **4FCH** remained unchanged with temperature (Fig. S20†), which indicates their normal fluorescent nature. These results imply that fluorene-based *o*-carboranyl compounds exhibit the TADF property, which is affected by the rigidity of their structural formation in accordance with the substitution position of the *o*-carborane cage in the fluorene plane. The TD-DFT calculation results for the S_1 states revealed that the orbital overlap-integral ($I_{H/L}$) between HOMO and LUMO levels for **4FC** was considerably lower (3.3%) than those for **2FC** (8.9%) and **3FC** (8.4%), which implies a discrete D–A structural feature. To verify the relationship between the structural fluctuation around the *o*-carborane cages and the TADF phenomenon, the energy gap (ΔE_{ST}) between the S_1 and T_1 states was estimated based on changes in the Ψ values for all *closo*-compounds (Fig. 5). The ΔE_{ST} value for **4FC** at Ψ = 90° is

nearly same as that (87.9°, Table 2) of the S_0-optimized structure; it is significantly small (0.032 eV). The result and the fact that **4FC** is fixed at around $\Psi = 90°$ because of the high-energy barrier suggests that **4FC** can maintain a small ΔE_{ST} in all states, which can sufficiently evoke an efficient TADF. The experimental ΔE_{ST} value for **4FC**, which is calculated using the gap of onset wavelengths for prompt and delayed PL (phosphorescent nature), was significantly similar (0.027 eV, Fig. S23†) to that value. To validate these small ΔE_{ST} values for **4FC** in both THF and the film state, ΔE_{ST} values were again calculated from the Arrhenius plots using the activation energy of the reverse intersystem crossing (RISC) (Fig. S24†). Indeed, temperature dependent rate constants of the RISC (k_{RISC}) were determined from the prompt and delayed fluorescence components and using previously reported equations.[82,83] Moreover, k_{RISC} in THF and the film at 298 K could be estimated as 4.0 and 3.5 × 10^7 s^{-1}, respectively. The ΔE_{ST} values evaluated from the slope of temperature dependence of the k_{RISC} plot (Arrhenius plot) was determined to be 8.9 meV in THF and 13.5 meV in the film. Thus, the narrow ΔE_{ST} value and relatively large k_{RISC} in both solution and the film support the efficient RISC process and TADF feature of **4FC**.

In contrast, ΔE_{ST} values for the other *closo*-compounds around each S_0-optimized structure ($\Psi \approx 90°$) were found to be greater than 0.10 eV; furthermore, those of **2FC** and **3FC** were found to be greater than 0.28 eV at $\Psi = 0°$. Based on the structural features of the compounds wherein the free rotation of *o*-carborane cages is comparatively easy to achieve owing to the low-energy barrier, these results indicate why *closo*-compounds besides **4FC** exhibit normal fluorescent characteristics in the film state.

Consequently, the strategic molecular design of *o*-carborane-appended fluorene compounds can lead to a rigid-structural formation, which enhances radiative efficiency for ICT transitions corresponding to *o*-carboranes and reveals their intriguing TADF nature.

Electrochemical and thermal stabilities of the *o*-carboranyl compounds

Electrochemical and thermal stabilities of organometallic materials are considerably important for wide practical applications. To obtain the stabilities for the *closo-o*-carboranyl compounds, **2FC–4FC**, cyclic voltammetry (CV) measurements (Fig. 6a), thermogravimetric analysis (TGA, Fig. 6b), and differential scanning calorimetry (DSC, Fig. 6b) were performed. The HOMO and LUMO energy levels for the compounds obtained using the measured oxidation ($V_{ox,onset}$, 1.39 V for **2FC**, 1.37 V for **3FC**, and 1.42 V for **4FC** → HOMO: −6.19 eV for **2FC**, −6.17 eV for **3FC**, and −6.22 eV for **4FC**) and reduction onset potentials ($V_{red,\ onset}$, −1.18 V for **2FC**, −1.23 V for **3FC**, and −1.27 V for **4FC** → LUMO: −3.62 eV for **2FC**, −3.57 eV for **3FC**, and −3.53 eV for **4FC**) were significantly similar to the HOMO levels on S_0-optimized structures and the LUMO levels on S_1-optimized structures obtained by TD-DFT calculations, respectively (Fig. 3, see the TD-DFT results). Furthermore, all the compounds underwent reversible and consistent oxidation and reduction processes during five consecutive cycles (Fig. S25†), implying outstanding electrochemical stability.

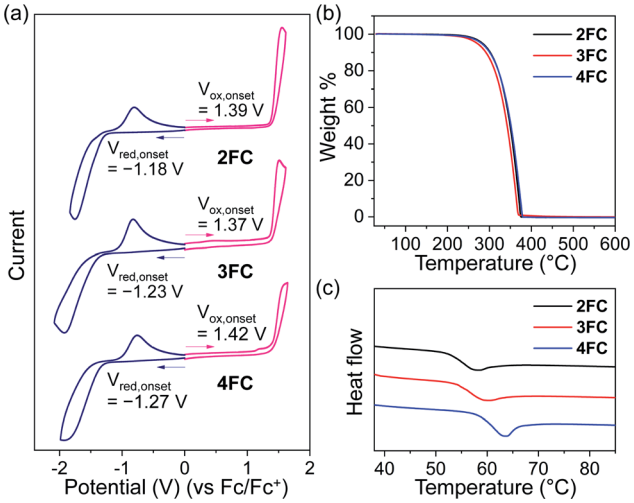

Fig. 6 (a) Cyclic voltammograms of **2FC**, **3FC**, and **4FC** showing oxidation (pink solid line) and reduction (navy) potentials (5 × 10^{-4} M in DCM, scan rate = 100 mV s^{-1}). (b) TGA and (c) DSC curves for **2FC**, **3FC**, and **4FC**.

The thermal stabilities of the compounds were investigated using T_{d5} (the temperature at 5 wt% degradation) and T_g (the glass transition temperature) values from TGA and DSC (Fig. 6b). **2FC**, **3FC**, and **4FC** exhibited relatively high T_{d5} and T_g values (284 °C and 58 °C for **2FC**, 271 °C and 61 °C for **3FC**, and 281 °C and 64 °C for **4FC**, respectively). These features could be attributed to the rigid and robust structure of the *closo-o*-carborane cluster. Consequently, these findings further support the potential of materials that can be applied to the optoelectronic industry.

Conclusions

We synthesized and characterized **2FC**, **3FC**, **4FC**, **4FCH**, and *nido*-**4FC**. The molecular structures for all *closo*-compounds were determined by single crystal X-ray diffraction analysis. The crystal structure of **4FC** exhibited a significantly distorted fluorene plane, which revealed severe intramolecular steric hindrance. Interestingly, **4FC** demonstrated intense ICT-based emission in all states (solution at 298 K and 77 K, film, and aggregated states), while other *closo*-compounds demonstrated emissions in only the rigid state. In addition, *nido*-**4FC** did not exhibit any emissive trace, which indicated that all radiative decay processes definitely corresponded to the ICT transition triggered by the existence of *closo-o*-carborane. Relative energy barriers and dihedral angles around *o*-carborane cages changed in *closo*-compounds, which indicated that *o*-carborane cages in all the compounds except for **4FC** could be freely rotated at ambient temperature, whereas the structural formation of **4FC** was fixed around its S_0-optimized structure. Furthermore, **4FC** demonstrated that separated PL decay components were short-lived (~0.5 ns) and long-lived (27–39 ns) in the solution at 298 K and in the film state, respectively, which could be attributed to

prompt fluorescence and TADF, respectively. Such a characteristic for **4FC** was revealed by maintaining the significantly small ΔE_{ST} in the structural fixation. Consequently, the strategic molecular design of the *o*-carborane-appended π-conjugated (D–A) system, which can form rigid structural geometries, can enhance radiative efficiency for ICT-based emission and trigger intriguing photophysical properties such as TADF. To the best of our knowledge, this is the first example of a *closo-o*-carboranyl D–A type compound demonstrating TADF nature in the solution state at ambient temperature; it demonstrates that the *closo-o*-carborane can act as a novel functional group of electronic acceptors for TADF.

Author contributions

D. K. You and H. So were responsible for experimental investigations and formal analysis (lead), data presentation, computational investigation, collected the X-ray data, solved the crystal structures, and visualization. C. H. Ryu and M. Kim were responsible for experimental investigations (supportive), computational investigation (lead) and visualization. K. M. Lee was in charge for methodology and conceptualization, computational investigations, writing original draft (lead), review and editing of the manuscript (lead), project administration and funding acquisition.

Conflicts of interest

There are no conflicts to declare.

Acknowledgements

This work was supported by the National Research Foundation of Korea (NRF) grant (NRF-2020R1A2C1006400 and NRF-2016M3A7B4909246 for K. M. Lee) funded by the Ministry of Science and ICT and Ministry of Education. We thank Dr Dongwook Kim (Center for Catalytic Hydrocarbon Functionalizations, Institute for Basic Science (IBS)) for assistance with X-ray diffraction experiments.

Notes and references

1 V. I. Bregadze, *Chem. Rev.*, 1992, **92**, 209–223.
2 F. Issa, M. Kassiou and L. M. Rendina, *Chem. Rev.*, 2011, **111**, 5701–5722.
3 R. Núñez, M. Tarrés, A. Ferrer-Ugalde, F. Fabrizi de Biani and F. Teixidor, *Chem. Rev.*, 2016, **116**, 14307–14378.
4 J. Ochi, K. Tanaka and Y. Chujo, *Angew. Chem., Int. Ed.*, 2020, **59**, 9841–9855.
5 M. F. Hawthorne, *Angew. Chem., Int. Ed.*, 1993, **32**, 950–984.
6 A. H. Soloway, W. Tjarks, B. A. Barnum, F. G. Rong, R. F. Barth, I. M. Codogni and J. G. Wilson, *Chem. Rev.*, 1998, **98**, 1515–1562.
7 M. F. Hawthorne and A. Maderna, *Chem. Rev.*, 1999, **99**, 3421–3434.
8 H. Jude, H. Disteldorf, S. Fischer, T. Wedge, A. M. Hawkridge, A. M. Arif, M. F. Hawthorne, D. C. Muddiman and P. J. Stang, *J. Am. Chem. Soc.*, 2005, **127**, 12131–12139.
9 Y. Shirai, J.-F. Morin, T. Sasaki, J. M. Guerrero and J. M. Tour, *Chem. Soc. Rev.*, 2006, **35**, 1043–1055.
10 B. P. Dash, R. Satapathy, E. R. Gaillard, J. A. Maguire and N. S. Hosmane, *J. Am. Chem. Soc.*, 2010, **132**, 6578–6587.
11 A. M. Spokoyny, C. W. Machan, D. J. Clingerman, M. S. Rosen, M. J. Wiester, R. D. Kennedy, C. L. Stern, A. A. Sarjeant and C. A. Mirkin, *Nat. Chem.*, 2011, **3**, 590–596.
12 Z. Qiu, S. Ren and Z. Xie, *Acc. Chem. Res.*, 2011, **44**, 299–309.
13 Z.-J. Yao and G.-X. Jin, *Coord. Chem. Rev.*, 2013, **257**, 2522–2535.
14 S. P. Fisher, A. W. Tomich, S. O. Lovera, J. F. Kleinsasser, J. Guo, M. J. Asay, H. M. Nelson and V. Lavallo, *Chem. Rev.*, 2019, **119**, 8262–8290.
15 K.-R. Wee, Y.-J. Cho, S. Jeong, S. Kwon, J.-D. Lee, I.-H. Suh and S. O. Kang, *J. Am. Chem. Soc.*, 2012, **134**, 17982–17990.
16 J. Guo, D. Liu, J. Zhang, J. Zhang, Q. Miao and Z. Xie, *Chem. Commun.*, 2015, **51**, 12004–12007.
17 R. Furue, T. Nishimoto, I. S. Park, J. Lee and T. Yasuda, *Angew. Chem., Int. Ed.*, 2016, **55**, 7171–7175.
18 R. Núñez, C. Viñas, F. Teixidor, R. Sillanpää and R. Kivekäs, *J. Organomet. Chem.*, 1999, **592**, 22–28.
19 F. Teixidor, R. Núñez, C. Viñas, R. Sillanpää and R. Kivekäs, *Angew. Chem., Int. Ed.*, 2000, **112**, 4460–4462.
20 R. Núñez, P. Farràs, F. Teixidor, C. Viñas, R. Sillanpää and R. Kivekäs, *Angew. Chem., Int. Ed.*, 2006, **45**, 1270–1272.
21 J. O. Huh, H. Kim, K. M. Lee, Y. S. Lee, Y. Do and M. H. Lee, *Chem. Commun.*, 2010, **46**, 1138–1140.
22 K. M. Lee, J. O. Huh, T. Kim, Y. Do and M. H. Lee, *Dalton Trans.*, 2011, **40**, 11758–11764.
23 K. Kokado and Y. Chujo, *J. Org. Chem.*, 2011, **76**, 316–319.
24 B. P. Dash, R. Satapathy, E. R. Gaillard, K. M. Norton, J. A. Maguire, N. Chug and N. S. Hosmane, *Inorg. Chem.*, 2011, **50**, 5485–5493.
25 K.-R. Wee, W.-S. Han, D. W. Cho, S. Kwon, C. Pac and S. O. Kang, *Angew. Chem., Int. Ed.*, 2012, **51**, 2677–2680.
26 L. Weber, J. Kahlert, R. Brockhinke, L. Böhling, A. Brockhinke, H.-G. Stammler, B. Neumann, R. A. Harder and M. A. Fox, *Chem. - Eur. J.*, 2012, **18**, 8347–8357.
27 A. Ferrer-Ugalde, E. J. uárez-Pérez, F. Teixidor, C. Viñas and R. Núñez, *Chem. - Eur. J.*, 2013, **19**, 17021–17030.
28 L. Weber, J. Kahlert, R. Brockhinke, L. Böhling, J. Halama, A. Brockhinke, H.-G. Stammler, B. Neumann, C. Nervi, R. A. Harder and M. A. Fox, *Dalton Trans.*, 2013, **42**, 10982–10996.
29 L. Weber, J. Kahlert, L. Böhling, A. Brockhinke, H.-G. Stammler, B. Neumann, R. A. Harder, P. Low and M. A. Fox, *Dalton Trans.*, 2013, **42**, 2266–2281.
30 S. Kwon, K.-R. Wee, Y.-J. Cho and S. O. Kang, *Chem. - Eur. J.*, 2014, **20**, 5953–5960.
31 H. J. Bae, H. Kim, K. M. Lee, T. Kim, Y. S. Lee, Y. Do and M. H. Lee, *Dalton Trans.*, 2014, **43**, 4978–4985.
32 J. Poater, M. Solà, C. Viñas and F. Teixidor, *Angew. Chem., Int. Ed.*, 2014, **53**, 12191–12195.
33 H. Naito, Y. Morisaki and Y. Chujo, *Angew. Chem., Int. Ed.*, 2015, **54**, 5084–5087.

34 B. H. Choi, J. H. Lee, H. Hwang, K. M. Lee and M. H. Park, *Organometallics*, 2016, **35**, 1771–1777.
35 S. Mukherjee and P. Thilagar, *Chem. Commun.*, 2016, **52**, 1070–1093.
36 J. Poater, M. Solà, C. Viñas and F. Teixidor, *Chem. - Eur. J.*, 2016, **22**, 7437–7443.
37 R. Núñez, I. Romero, F. Teixidor and C. Viñas, *Chem. Soc. Rev.*, 2016, **45**, 5147–5173.
38 K. O. Kirlikovali, J. C. Axtell, A. Gonzalez, A. C. Phung, S. I. Khan and A. M. Spokoyny, *Chem. Sci.*, 2016, **7**, 5132–5138.
39 H. Naito, K. Nishino, Y. Morisaki, K. Tanaka and Y. Chujo, *J. Mater. Chem. C*, 2017, **5**, 10047–10054.
40 D. Tu, P. Leong, S. Guo, H. Yan, C. Lu and Q. Zhao, *Angew. Chem., Int. Ed.*, 2017, **56**, 11370–11374.
41 K. Nishino, K. Uemura, K. Tanaka, Y. Morisaki and Y. Chujo, *Eur. J. Org. Chem.*, 2018, **12**, 1507–1512.
42 H. Mori, K. Nishino, K. Wada, Y. Morisaki, K. Tanaka and Y. Chujo, *Mater. Chem. Front.*, 2018, **2**, 573–579.
43 I. Nar, A. Atsay, A. Altındal and E. Hamuryudan, *Inorg. Chem.*, 2018, **57**, 2199–2208.
44 H. Jin, H. J. Bae, S. Kim, J. H. Lee, H. Hwang, M. H. Park and K. M. Lee, *Dalton Trans.*, 2019, **48**, 1467–1476.
45 K. L. Martin, J. N. Smith, E. R. Young and K. R. Carter, *Macromolecules*, 2019, **52**, 7951–7960.
46 K.-R. Wee, Y.-J. Cho, J. K. Song and S. O. Kang, *Angew. Chem., Int. Ed.*, 2013, **52**, 9682–9685.
47 A. Ferrer-Ugalde, A. González-Campo, C. Viñas, J. Rodríguez-Romero, R. Santillan, N. Farfán, R. Sillanpää, A. Sousa-Pedrares, R. Núñez and F. Teixidor, *Chem. - Eur. J.*, 2014, **20**, 9940–9951.
48 K. Nishino, H. Yamamoto, K. Tanaka and Y. Chujo, *Org. Lett.*, 2016, **18**, 4064–4067.
49 K. Nishino, H. Yamamoto, K. Tanaka and Y. Chujo, *Asian J. Org. Chem.*, 2017, **6**, 1818–1822.
50 H. Naito, K. Nishino, Y. Morisaki, K. Tanaka and Y. Chujo, *Angew. Chem., Int. Ed.*, 2017, **56**, 254–259.
51 X. Wu, J. Guo, Y. Cao, J. Zhao, W. Jia, Y. Chen and D. Jia, *Chem. Sci.*, 2018, **9**, 5270–5277.
52 J. Li, C. Yang, X. Peng, Y. Chen, Q. Qi, X. Luo, W.-Y. Lai and W. Huang, *J. Mater. Chem. C*, 2018, **6**, 19–28.
53 X. Wu, J. Guo, J. Zhao, Y. Che, D. Jia and Y. M. Chen, *Dyes Pigm.*, 2018, **154**, 44–51.
54 A. V. Marsh, N. J. Cheetham, M. Little, M. Dyson, A. J. P. White, P. Beavis, C. N. Warriner, A. C. Swain, P. N. Stavrinou and M. Heeney, *Angew. Chem., Int. Ed.*, 2018, **57**, 10640–10645.
55 S. Kim, J. H. Lee, H. So, J. Ryu, J. Lee, H. Hwang, Y. Kim, M. H. Park and K. M. Lee, *Chem. - Eur. J.*, 2020, **26**, 548–557.
56 S. Kim, J. H. Lee, H. So, M. Kim, M. S. Mun, H. Hwang, M. H. Park and K. M. Lee, *Inorg. Chem. Front.*, 2020, **7**, 2949–2959.
57 N. Shin, S. Yu, J. H. Lee, H. Hwang and K. M. Lee, *Organometallics*, 2017, **36**, 1522–1529.
58 H. So, J. H. Kim, J. H. Lee, H. Hwang, D. K. An and K. M. Lee, *Chem. Commun.*, 2019, **55**, 14518–14521.
59 M. Kim, C. H. Ryu, J. H. Hong, J. H. Lee, H. Hwang and K. M. Lee, *Inorg. Chem. Front.*, 2020, **7**, 4180–4189.
60 Q. Zhang, J. Li, K. Shizu, S. Huang, S. Hirata, H. Miyazaki and C. Adachi, *J. Am. Chem. Soc.*, 2012, **134**, 14706–14709.
61 K. Goushi, K. Yoshida, K. Sato and C. Adachi, *Nat. Photonics*, 2012, **6**, 253–258.
62 H. Uoyama, K. Goushi, K. Shizu, H. Nomura and C. Adachi, *Nature*, 2012, **492**, 234–238.
63 Y. Tao, K. Yuan, T. Chen, P. Xu, H. Li, R. Chen, C. Zheng, L. Zhang and W. Huang, *Adv. Mater.*, 2014, **26**, 7931–7958.
64 M. Y. Wong and E. Zysman-Colman, *Adv. Mater.*, 2017, **29**, 1605444.
65 Z. Yang, Z. Mao, Z. Xie, Y. Zhang, S. Liu, J. Zhao, J. Xu, Z. Chi and M. P. Aldred, *Chem. Soc. Rev.*, 2017, **46**, 915–1016.
66 F. B. Dias, K. N. Bourdakos, V. Jankus, K. C. Moss, K. T. Kamtekar, V. Bhalla, J. Santos, M. R. Bryce and A. P. Monkman, *Adv. Mater.*, 2013, **25**, 3707–3714.
67 Q. Zhang, B. Li, S. Huang, H. Nomura, H. Tanaka and C. Adachi, *Nat. Photonics*, 2014, **8**, 326–332.
68 H. Kaji, H. Suzuki, T. Fukushima, K. Shizu, K. Suzuki, S. Kubo, T. Komino, H. Oiwa, F. Suzuki, A. Wakamiya, Y. Murata and C. Adachi, *Nat. Commun.*, 2015, **6**, 8476.
69 S. Hirata, Y. Sakai, K. Masui, H. Tanaka, S. Y. Lee, H. Nomura, N. Nakamura, M. Yasumatsu, H. Nakanotani, Q. Zhang, K. Shizu, H. Miyazaki and C. Adachi, *Nat. Mater.*, 2015, **14**, 330–336.
70 M. Z. Shafikov, A. F. Suleymanova, R. Czerwieniec and H. Yersin, *Chem. Mater.*, 2017, **29**, 1708–1715.
71 J. Llop, C. Viñas, F. Teixidor, L. Victori, R. Kivekäs and R. Sillanpää, *Organometallics*, 2001, **20**, 4024–4030.
72 J. M. Oliva, N. L. Allan, P. v. R. Schleyer, C. Viñas and F. Teixidor, *J. Am. Chem. Soc.*, 2005, **127**, 13538–13547.
73 A. Ferrer-Ugalde, E. J. Juárez-Pérez, F. Teixidor, C. Viñas, R. Sillanpää, E. Pérez-Inestrosa and R. Núñez, *Chem. - Eur. J.*, 2012, **18**, 544–553.
74 M. J. Frisch, G. W. Trucks, H. B. Schlegel, G. E. Scuseria, M. A. Robb, J. R. Cheeseman, G. Scalmani, V. Barone, G. A. Petersson, H. Nakatsuji, X. Li, M. Caricato, A. V. Marenich, J. Bloino, B. G. Janesko, R. Gomperts, B. Mennucci, H. P. Hratchian, J. V. Ortiz, A. F. Izmaylov, J. L. Sonnenberg, D. Williams-Young, F. Ding, F. Lipparini, F. Egidi, J. Goings, B. Peng, A. Petrone, T. Henderson, D. Ranasinghe, V. G. Zakrzewski, J. Gao, N. Rega, G. Zheng, W. Liang, M. Hada, M. Ehara, K. Toyota, R. Fukuda, J. Hasegawa, M. Ishida, T. Nakajima, Y. Honda, O. Kitao, H. Nakai, T. Vreven, K. Throssell, J. A. Montgomery, Jr, J. E. Peralta, F. Ogliaro, M. J. Bearpark, J. J. Heyd, E. N. Brothers, K. N. Kudin, V. N. Staroverov, T. A. Keith, R. Kobayashi, J. Normand, K. Raghavachari, A. P. Rendell, J. C. Burant, S. S. Iyengar, J. Tomasi, M. Cossi, J. M. Millam, M. Klene, C. Adamo, R. Cammi, J. W. Ochterski, R. L. Martin, K. Morokuma, O. Farkas, J. B. Foresman and D. J. Fox, *Gaussian 16 Revision B.01*; Gaussian. Inc., Wallingford, CT, 2016.
75 E. Runge and E. K. U. Gross, *Phys. Rev. Lett.*, 1984, **52**, 997–1000.

76 S. Miertuš, E. Scrocco and J. Tomasi, *Chem. Phys.*, 1981, **55**, 117–129.
77 N. M. O'Boyle, A. L. Tenderholt and K. M. Langner, *J. Comput. Chem.*, 2008, **29**, 839–845.
78 R. Dennington, T. A. Keith and J. M. Millam, *GaussView 6*, Semichem Inc., Shawnee Mission, KS, 2016.
79 M. F. Hawthorne, T. E. Berry and P. A. Wegner, *J. Am. Chem. Soc.*, 1965, **87**, 4746–4750.
80 T. E. Paxson, K. P. Callahan and M. F. Hawthorne, *Inorg. Chem.*, 1973, **12**, 708–709.
81 W. Jiang, C. B. Knobler and M. F. Hawthorne, *Inorg. Chem.*, 1996, **35**, 3056–3058.
82 L. Zhang and K. W. Cheah, *Sci. Rep.*, 2018, **8**, 8832.
83 K. J. Kim, G. H. Kim, R. Lampande, D. H. Ahn, J. B. Im, J. S. Moon, J. K. Lee, J. Y. Lee, J. Y. Lee and J. H. Kwon, *J. Mater. Chem. C*, 2018, **6**, 1343–1348.